NANO LETTERS

pubs.acs.org/NanoLett Letter

Atomistic Positioning of Defects in Helium Ion Treated Single-Layer MoS_2

Elmar Mitterreiter, Bruno Schuler, Katherine A. Cochrane, Ursula Wurstbauer, Alexander Weber-Bargioni, Christoph Kastl, and Alexander W. Holleitner*

Cite This: *Nano Lett.* 2020, 20, 4437−4444 Read Online

ACCESS | Metrics & More | Article Recommendations | Supporting Information

ABSTRACT: Structuring materials with atomic precision is the ultimate goal of nanotechnology and is becoming increasingly relevant as an enabling technology for quantum electronics/spintronics and quantum photonics. Here, we create atomic defects in monolayer MoS_2 by helium ion (He-ion) beam lithography with a spatial fidelity approaching the single-atom limit in all three dimensions. Using low-temperature scanning tunneling microscopy (STM), we confirm the formation of individual point defects in MoS_2 upon He-ion bombardment and show that defects are generated within 9 nm of the incident helium ions. Atom-specific sputtering yields are determined by analyzing the type and occurrence of defects observed in high-resolution STM images and compared with Monte Carlo simulations. Both theory and experiment indicate that the He-ion bombardment predominantly generates sulfur vacancies.

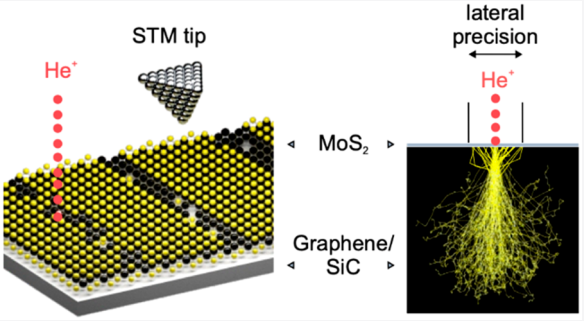

KEYWORDS: *Two-dimensional materials, defect engineering, scanning tunneling microscopy, helium ion microscopy*

Atomically precise manufacturing is considered a key enabling technology for on-chip quantum photonics and quantum electronics/spintronics. Examples include the deterministic creation of quantum emitters[1] and their positioning in photonic circuits,[2] single-atom transistors,[3] and atomic spin qubits.[4] Controlling the interaction between such atomic quantum systems and exploiting collective phenomena ultimately requires a deterministic, atomic-scale placement control in all three dimensions. Ion beam implantation techniques are widely used to create optically active quantum emitters, commonly referred to as color centers, with high spatial resolution in materials including diamond[5−8] and sodium chloride.[9] Such atomistic defects can serve as single photon sources with very narrow optical line widths and small ensemble broadening.[5−8] This stands in contrast to mesoscopic emitters, such as quantum dots and strain islands, where variations of the confinement potential result in randomly varying optoelectronic properties.[10−12] However, the degree to which the implantation of atomistic defects in bulk materials can be controlled, both laterally and vertically, is fundamentally limited by the stochastic interaction between the ion beam and the host lattice. Two-dimensional (2D) materials, such as molybdenum disulfide (MoS_2), can help overcome the latter limitation, because on the one hand they provide an intrinsic subnanometer confinement for the implanted defects in the vertical direction, and on the other hand the lateral broadening of the ion beam is reduced in thin films.[13,14] Furthermore, the interfacial nature of 2D materials provides opportunities to access, utilize, and even combine different defect types in a controlled manner and to engineer functionality in these materials. Highly focused ion beams for nanopatterning of single-layer MoS_2 using gold,[15] xenon,[16] or argon[17] were shown to provide a lateral precision below 15 nm. Even higher spatial resolution can ultimately be achieved for suspended layers, such as graphene monolayers, bombarded with helium ions[18−20] or patterned in a transmission electron microscope (TEM).[21,22] However, TEM is difficult to scale due to its low focal depth, the limited field of view, and the lack of a substrate which hinders the fabrication of more complex structures. Importantly, focused helium-ion (He-ion) bombardment can be used to deterministically implant single photon emitters in heterostructures composed of hBN and single-layer MoS_2, as we have recently shown.[13] The emitters exhibit a microsecond lifetime at low temperatures and can be generated in the MoS_2 layer with a high yield and improved spectral homogeneity due to the encapsulation between inert hBN layers.[13,23,24] However, a thorough, atomistic understanding of the type and distribution of defects generated under focused He-ion irradiation is still lacking.

Received: March 19, 2020
Revised: April 30, 2020
Published: May 5, 2020

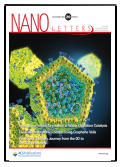

Downloaded via UNIV OF NORTH TEXAS on December 18, 2020 at 08:51:00 (UTC).
See https://pubs.acs.org/sharingguidelines for options on how to legitimately share published articles.

ACS Publications © 2020 American Chemical Society

https://dx.doi.org/10.1021/acs.nanolett.0c01222
Nano Lett. 2020, 20, 4437−4444

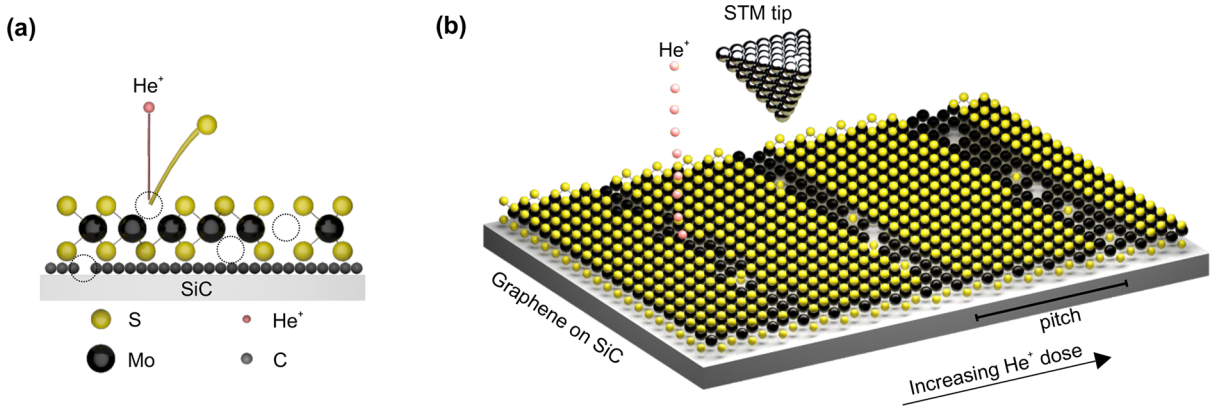

Figure 1. Atomic-scale ion patterning and imaging of 2D materials. (a) Schematic of single-layer MoS_2 on graphene/SiC under He-ion irradiation (side view). The incident helium ions sputter the sample and create different types of defects. Exemplarily, top and bottom sulfur vacancies, a molybdenum vacancy, as well as defects in the graphene layer are visualized and highlighted with black circles. (b) Line arrays of defects with pitch of 20 nm and well-defined defect density are created deterministically by the focused ion beam. STM images the patterns with atomic resolution.

We pattern atomistic defects in monolayer MoS_2 by helium ion microscopy (HIM) and subsequently use atomic resolution scanning probe microscopy to directly uncover defect statistics and their electronic structure on the atomic scale. We demonstrate a lateral precision of 9 nm (full width at half-maximum (fwhm)) for defects implanted into supported 2D MoS_2. By comparing pristine and He-ion treated MoS_2, we quantify the occurrence of different defects, and for unencapsulated MoS_2, we identify the most prominent ones as oxygen passivated sulfur vacancies. Ultimately, our approach helps to bridge the observations made in typical macroscopic or ensemble measurements, such as optical or photoemission spectroscopy,[23,25,26] with the insights from structural and electronic characterization at the atomic scale.[27,28] Our combined HIM/scanning tunneling microscopy (STM) work demonstrates that optically active point defects can be integrated into nanophotonic devices with almost atomic precision.

Figure 1 shows a schematic of our atomistic defect generation and imaging. We show common point defects which occur upon He-ion bombardment of single-layer MoS_2 on the graphene/SiC support: top and bottom sulfur vacancies, a molybdenum vacancy, and point defects in the graphene substrate (Figure 1a). We note that, in general, a large variety of different point defects or more complex defect clusters could be present in MoS_2, such as double vacancies, anti-site defects, interstitials or substitutional defects.[21,29−31] We use the HIM to imprint point defects along lines into the MoS_2 layer (Figure 1b), with a spot size of 0.5 nm at the surface of the patterned material. The high energy of the ions combined with their small masses results in a highly focused ion beam that can be used to implant defects even into readily assembled 2D heterostructures of MoS_2 and an hBN encapsulation layer.[13]

Three different types of samples consisting of MoS_2 transferred on graphene/SiC were studied: (i) pristine MoS_2 as a control sample, (ii) MoS_2 bombarded homogeneously across the whole flake with a constant ion dose of 5×10^{14} cm^{-2}, and (iii) MoS_2 bombarded with helium ions along parallel lines. For the patterned sample (iii), we created arrays consisting of 12 lines of 40 μm length and 20 nm pitch between the lines. For each line, the He-ion dose was kept constant. Within each array, we increased the ion dose successively from 10 ions/nm to 1000 ions/nm between the lines (cf. Figure 1b). Subsequently, the line arrays were repeated across the whole flake. After the He-ion patterning, we imaged the different samples using low-temperature STM and scanning tunneling spectroscopy (STS) at $T = 6$ K (Figure 1b). All STM images were recorded in constant current mode with a tunneling current set point of $I_t = 100$ pA.

Figure 2a shows a large-scale STM image of single-layer MoS_2 patterned with line arrays. In the image, circular black features with a lateral extent of about 2 nm are observed. As discussed later, these black features correspond to charged defects.[28,32] Although other ion-induced defects are present, and even more abundant, the large-scale image contrast is dominated by these charged defects. As evident from Figure 2a, the defects align vertically (indicated by dashed lines) with a spacing of approximately 20 nm, consistent with the pitch of the exposed line patterns. The defect density increases from left to right, consistent with the corresponding increase of the He-ion dose in the exposure pattern. Thus, we identify the observed features as the lines from the previous exposure to the He-ion beam. Additionally, we observe bright spots whose density also correlates with the He-ion dose. These features are most likely surface adsorbates originating from either polymer residues from the dry transfer of MoS_2 or redeposited sputtered material. Presumably, the adsorbates diffuse on the surface and preferentially bond to HIM-induced defects that constitute reactive sites. The adsorbates are frequently displaced or picked up by the tip making their close inspection challenging (cf. Supporting Information).

To statistically analyze the spatial distribution in more detail, we extract the lateral coordinates of the easily visible, charged defects both manually and automatically by an image analysis protocol (cf. Supporting Information). Figure 2b shows a histogram of the distribution of the charged defects across the HIM lines, exhibiting five maxima corresponding to five different He-ion doses. From this histogram, we calculate the sputtering yield defined as the integrated number of defects for every line divided by the corresponding line dose (cf. Table 1). The Gaussian probability distributions for the line shape fitted to the histogram data are plotted in yellow. We use a maximum likelihood estimator for each of the accumulated defect lines and assume underlying Poissonian statistics of the defect counts (cf. Supporting Information). From this analysis, we extract a fwhm of (9.3 ± 1.8) nm and an averaged spacing of the lines of (18.9 ± 2.7) nm, which is in good agreement with the anticipated pitch of 20 nm. Several independent samples

https://dx.doi.org/10.1021/acs.nanolett.0c01222
Nano Lett. 2020, 20, 4437−4444

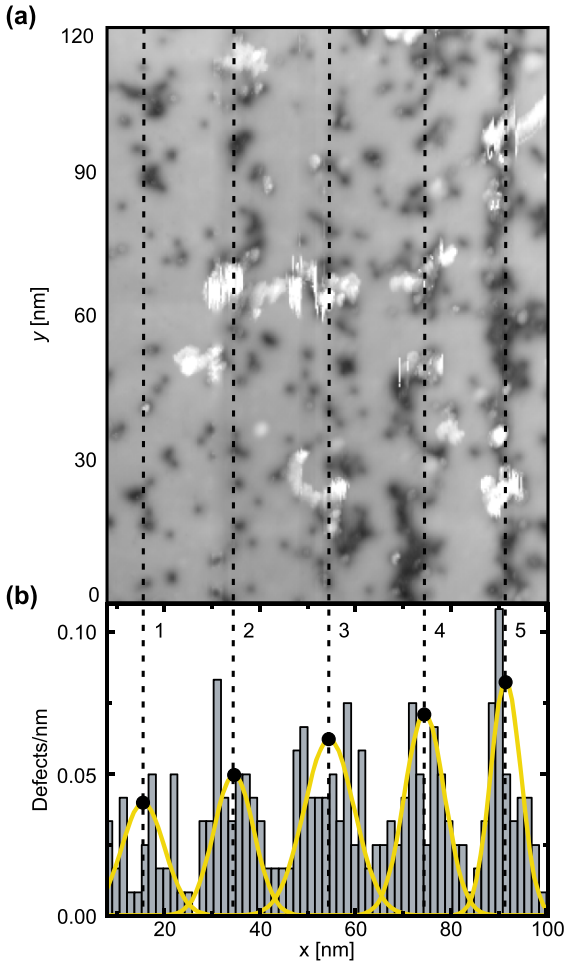

Figure 2. He-ion-induced line patterns in single-layer MoS_2. (a) STM topography of HIM patterned single-layer MoS_2. The ion-induced defects are arranged in a vertical line array with a pitch of 20 nm (black dashed lines), as expected. Ion dose and corresponding defect density increase toward the right. The most apparent defects (type A) appear as dark depressions. White, streaky areas correspond to surface adsorbates. (b) Spatial distribution of HIM-induced defects. Yellow lines are Gaussian fits, and black dashed lines indicate the fitted mean. Imaging parameters: V_b = 0.5 V, I_t = 100 pA, 100 nm × 120 nm.

show an averaged line spacing of (18.9 ± 2.8) nm and an averaged fwhm of (8.8 ± 1.7) nm (cf. Table 1). Our results demonstrate a high degree of positional and density control over defect generation. However, the line patterns are rather broad (8.8 ± 1.7) nm as compared to the minimum width of the incident He-ion beam (0.5 nm).[33] In an independent study, Pöpsel et al. showed that the imaging resolution of the same HIM is at <2 nm.[34] In a control measurement, we determine an upper bound for the beam diameter of 1.9 nm (fwhm) for our instrument under equivalent conditions (cf. Supporting Information). Consequently, the approximately 9 nm broad defect distribution cannot be attributed to the extent of the incident He-ion beam. A previous numerical study suggests that at ion energies of 30 keV and perpendicular ion irradiation of the MoS_2 backscattered helium ions and sputtered substrate atoms create most defects within a circular area of 8 nm diameter around the impact point.[14] This number is in very good agreement with our observed line width of (8.8 ± 1.7) nm. We conclude that mainly the supporting substrate limits the spatial precision of defect generation. Suspended

Table 1. Statistics of HIM Patterned Lines[a]

line	helium ion dose (ions/nm)	integrated number of defects (nm^{-1})	sputtering yield (10^{-3})	lateral fwhm (nm)	center (nm)
1	60	0.350	5.8	9.3 ± 1.7	15.4
2	80	0.475	5.9	8.7 ± 1.3	34.5
3	100	0.575	5.8	11.2 ± 1.6	54.6
4	125	0.517	4.1	9.8 ± 0.8	74.5
5	150	0.467	3.1	7.7 ± 0.9	91.3

[a]Applied He-ion dose, corresponding number of defects normalized to the length of the line (120 nm), and resulting sputtering yield for the lines shown in Figure 2 as well as the FWHM and the center position of the fitted Gaussian distributions. For low He-ion doses up to 100 ions/nm, the sputtering yield is constant with a value of 5.8 × 10^{-3}. For ion doses >100 ions/nm, a systematic error in counting the charged defects at higher density due to the overlap of their spatial extent in the image or due to the increase of adsorbates seems to mask the defects underneath.

MoS_2 layers would avoid backscattering of impinging ions and reduce the effective sputter radius, as demonstrated for milling of suspended MoS_2 and recently also graphene.[18−20,22,35] Then, in combination with the demonstrated high control over the number of defects via the He-ion dose, few to single defects could be placed deterministically with a lateral precision below 2 nm.

Having demonstrated the lateral precision of the HIM-induced defect patterns, we investigate the various types of defects by examining a homogeneously bombarded MoS_2 flake (5 × 10^{14} cm^{-2} corresponding to lowest line dose). We consistently observe six types of defects, which we label A−F (Figure 3a). Figure 3b shows high-resolution STM images of each of the commonly observed defects. Defect A shows a spherical shape, which we assign to a negatively charged point defect.[28,32] The long-range Coulomb potential of the charged defect dominates the overall STM signal, which masks the chemical defect states. Defect B occurs in two configurations, which will be discussed below. Due to the underlying trigonal symmetry of the MoS_2 lattice, hexagonal and trigonal defect orbitals, such as those seen in defects C and D, are consistent with simple point defects, such as monovacancies or substitutional defects. The symmetries of defect E and F do not align with the crystal symmetry and likely represent lower symmetry or composite defects, observed here for the first time in STM.

For each of the six defect types, we determine their occurrences in more than 70 STM overview images (total area: 1.3 × 10^4 nm^2), for randomly selected positions on several independent samples. For each image, we normalize the number of defects to the total scan size and calculate the sputtering yields with the known exposure dose. To accurately determine the sputtering yield, we study untreated MoS_2 control samples to obtain the pristine defect densities to correct the defect densities after HIM treatment (see Supporting Information). In pristine MoS_2, we predominantly observe defects of type B (cf. Figure 3b) distributed homogeneously over the sample. Their density is (3.5 ± 0.8) × 10^{12} cm^{-2}, which is in good agreement with previously reported defect densities of pristine, mechanically exfoliated MoS_2 of around (4.6 ± 1.0) × 10^{12} cm^{-2}[37] and (5−50) × 10^{12} cm^{-2}.[38] Defects A, C, D, E and F are absent in pristine MoS_2, within our experimental statistics.

https://dx.doi.org/10.1021/acs.nanolett.0c01222
Nano Lett. 2020, 20, 4437−4444

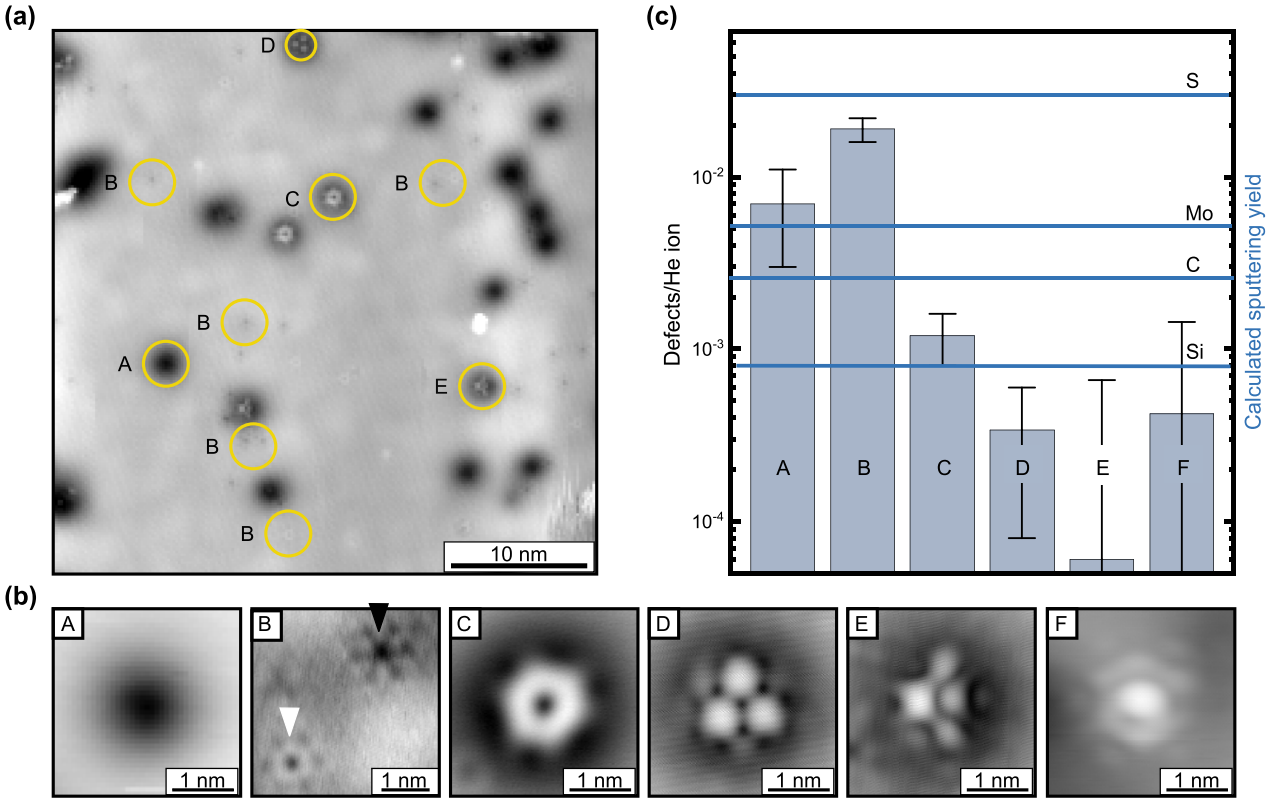

Figure 3. He-ion-induced defects in single-layer MoS_2. (a) STM overview scan of He-ion bombarded MoS_2. Yellow circles labeled A−E highlight the most frequently induced defects (F is not visible in this scan). (b) High-resolution STM topography of all observed defects A−F. Defect B occurs in two different configurations highlighted with a black and white triangle. B is the only defect also found in pristine MoS_2. (c) Bars show the experimentally observed number of defects A−F per incident helium ion. Blue lines represent Monte Carlo simulated sputtering yields (using the SRIM/TRIM package)[36] for all possibly sputtered atoms: sulfur, molybdenum, carbon, and silicon. Imaging parameters: V_b = 0.45 V, I_t = 100 pA.

Upon He-ion irradiation, the most frequently observed defect is type B, with a background corrected density of $(9.6 \pm 1.6) \times 10^{12}$ cm^{-2}. We can identify the two configurations of defect B (cf. Figure 3b black and white triangle) as oxygen saturated top and bottom sulfur vacancies by their characteristic image contrast in STM as well as AFM (cf. Supporting Information Figure S4) and the lack of in-gap states.[27,28] Intriguingly, pristine sulfur vacancies are absent in the as exfoliated control samples, where we predominantly find such oxygen substitutional defects, similar to recent studies on CVD grown WS_2[39] and MBE grown $MoSe_2$.[27] A further consequence is that, while sulfur vacancies are likely the predominant defect generated by the ion bombardment under vacuum conditions, they apparently become passivated in our uncapped MoS_2 layers, presumably during the transfer and handling in atmosphere between ion bombardment and STM imaging.

In the histogram (Figure 3c), the blue lines denote theoretical sputtering yields determined by Monte Carlo binary collision approximation simulations (SRIM/TRIM software package)[36] for all present elements: sulfur, molybdenum, carbon, and silicon. The scattering integral between the incident helium ions and the sample is solved classically, and the energy loss of the ions as well as the scattering angle are obtained for every collision. Stable defects are formed, if an energy higher than the threshold displacement energy is transferred to the crystal. According to the calculations, the most frequently sputtered element is expected to be sulfur, followed by molybdenum and carbon. The sputtering yield for silicon is almost 2 orders of magnitude below the sputtering yield of sulfur. The experimental sputtering yield of $(19 \pm 3) \times 10^{-3}$ (Table 2 and Figure 3c) for the oxygen passivated sulfur vacancy (type B) is in good agreement with the reported theoretical sputtering yield of 21×10^{-3} (24×10^{-3} on SiO_2)[14] for sulfur, and in the same order of magnitude as our Monte Carlo simulations of about 30×10^{-3}. Type A is the second most frequent defect with a sputtering yield of approximately 6×10^{-3}. Overall, the sputtering yield agrees reasonably with the calculated sputtering yield for molybdenum atoms. However, the exact identification of these charged defects is very challenging, since the STM contrast and STS spectra are dominated by the charge state of the defect and do not provide an informative chemical fingerprint. To uncover the structure of these charged defects, we conducted preliminary AFM measurements, which indicate the presence of a variety of different and more complex defect structures. The full classification of these charged defects requires further experiments that go beyond the scope of the present manuscript. Although we find correlations between calculated sputtering yields and abundance for other types of defects, we cannot conclusively identify them based on this criterion alone. The possible formation of more complex defects containing several individual point defects hinders the classification.[21,29−31] Furthermore, we do not know the influence of sputtered substrate atoms, that is, defects below the MoS_2 layer on its electronic structure. The hexagonal and trigonal symmetries of defects C and D indicate the presence of rather

https://dx.doi.org/10.1021/acs.nanolett.0c01222
Nano Lett. 2020, 20, 4437−4444

Table 2. Experimentally Determined Defect Density and Resulting Sputtering Yield for All Observed Defect Types on Large-Area HIM Bombarded MoS_2[a]

defect type	defect density (10^{12} cm^{-2})	experimental sputtering yield per He ion (10^{-3})
pristine defect density (O_S)	3.5 ± 0.8	–
defect A (charged)	3.4 ± 1.9	7 ± 4
defect B (O_S) background corrected	9.6 ± 1.6	19 ± 3
defect C	0.60 ± 0.21	1.2 ± 0.4
defect D	0.17 ± 0.13	0.34 ± 0.26
defect E	0.03 ± 0.30	0.06 ± 0.60
defect F	0.21 ± 0.51	0.42 ± 1.02

[a]Defect B is also found in pristine MoS_2. Therefore, the density of type B after HIM bombardment is corrected for the measured background defect density of pristine MoS_2.

simple point defects, likely related to nonpassivated sulfur vacancies.

The defects we labeled types E and F are rare, and they can be only observed in a limited number of STM images. Consequently, the standard deviation used to calculate the error bars in Figure 3c is comparably high. While we believe that these defects do not impact any macroscopic functionality, we added them to provide a complete description of this atomic-scale defect engineering process. The electronic structure characterizations via STS measurements on defects C−F show the presence of additional in-gap states for defects C, D, and F (see Supporting Information Figure 5). However, defects A and C, D, and E appear as negatively charged in the STM study due to the band alignment of MoS_2 and graphene, as can be seen from the dark halos around the defects in the STM contrast.[32] Consequently, the interpretation of the observed resonances is not as straightforward compared to, for example, neutral sulfur vacancies in WS_2/graphene.[39] Further studies, for example, on gated devices are required, to provide a complete picture of the defect's electronic structure.

Recently, we studied pristine and HIM treated MoS_2[23] and observed single photon emission from single defects after the He-ion treatment.[13,24] Furthermore, HIM-induced defects activate the inert basal plane of MoS_2 toward the catalytic hydrogen evolution reaction.[40] So far, the exact nature of these observed effects is not clear. However, oxygen passivated sulfur vacancies (defect B) cannot be responsible for the observed emission or the catalytic activity, as they are also present in pristine MoS_2. Possible defects could be molybdenum vacancies, defect complexes, or nonoxygen passivated sulfur vacancies, whereby previous encapsulation of MoS_2 in hBN and subsequent ion bombardment, as applied for example in ref 13, might protect unsaturated dangling bonds of ion-induced defects.

For technical applications, crucial aspects are the minimum spatial resolution at which defects can be implanted with high yield and scalability. Figure 4 compares lateral and vertical precision of different fabrication techniques for the creation of functional defects in different material systems, including the presented maskless HIM method for 2D materials. Due to their atomic out-of-plane confinement, 2D materials offer a natural advantage over three-dimensional (3D) materials, where defects are often buried tens of nanometer below the surface in the bulk, even with sophisticated implantation techniques. Nevertheless, color centers in different host

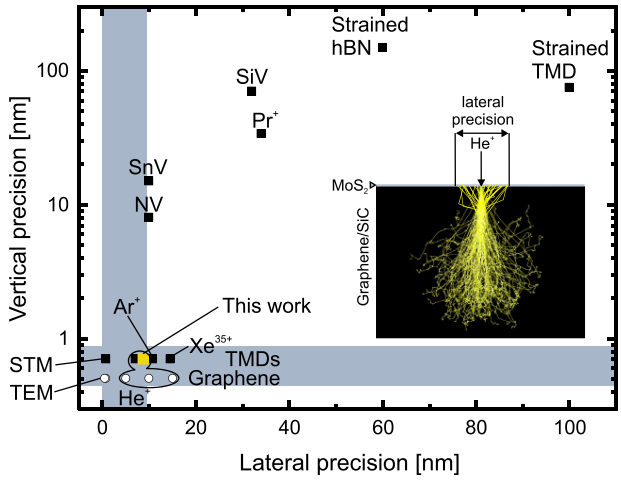

Figure 4. Precision of deterministically created defects. Lateral and vertical precision of defect creation for different techniques. Shaded areas represent lateral atomic precision and vertical sub-10 nm precision. The yellow square shows the precision of our HIM approach. The inset represents exemplarily the simulated interaction volume of an initially 0.5 nm wide He-ion beam interacting with a single-layer MoS_2 supported by graphene/SiC. Backscattered helium ions and substrate atoms can sputter the MoS_2 and decrease the lateral precision as indicated by the arrow.

crystals created by ion bombardment with silicon,[5] tin,[41] praseodymium,[42] or nitrogen[6−8] exhibit a high lateral precision due to the use of hard masking or focused ion beam techniques. Strain-induced quantum emitters in 2D WS_2, WSe_2, and hBN are likely created via a combination of the mesoscopic 3D strain potentials and local point defects. They exhibit also a low lateral precision due to insufficient control over the occurrence of the active defect sites.[1,43] We note that, although the TMD host crystals are atomically thin, the nonplanarity of the strain inducing nanopillars poses a lower limit for the overall height of the structure. Therefore, we define the latter to describe their vertical precision. By contrast, the vertical precision of defects generated in planar 2D materials is readily below 1 nm. The bottom left part of Figure 4 indicates the precision of STM-induced desorption[44] as well as xenon,[16] argon,[17] and helium[45] ion bombardment of single-layer MoS_2 (black squares) together with helium ion[18−20] and TEM treated[22] suspended graphene (white circles). The yellow square shows the precision of our HIM approach in single-layer MoS_2 supported on graphene/SiC. For 2D materials supported on a substrate, backscattered helium ions and substrate atoms broaden the effective interaction cross section at the 2D material, even for beam diameters as small as 0.5 nm (cf. inset of Figure 4). For suspended layers, including graphene and MoS_2 layers, the absence of backscattering from the substrate explains the enhanced lateral precision observed with He-ion and electron bombardment.[18−20,22,35] In principle, the best lateral precision on the atomic scale is reached for manipulation of surface atoms in STM[46] and beam-induced defect generation in TEM, whereby the latter has in principle subangstrom resolution. However, due to their limited field of view and incompatibility with existing wafer processing technologies, STM and TEM are not amenable to defect creation on larger device scales, and they are of minor relevance for technological applications. By contrast, defect creation using a HIM is fast (~10^5 defects per second at 1 pA beam current), compatible with existing wafer technology, and

https://dx.doi.org/10.1021/acs.nanolett.0c01222
Nano Lett. 2020, 20, 4437−4444

hence ultimately scalable. For our study, we created point defects arranged along 40 μm long line arrays with a lateral resolution of around 9 nm. We anticipate that the lateral resolution can be improved to ~1 nm for suspended 2D materials. Nevertheless, combining the previously reported capability to implant spectrally narrow quantum emitters into preassembled heterostructures, for example, hBN/MoS_2/hBN,[24] by HIM and the now demonstrated lateral resolution <10 nm open exciting possibilities for applications in quantum nanophotonics. In particular, such quantum emitters might be positioned at locations with optimized field distributions and coupling strengths within optical cavities or in close distance to each other to enable an optical interdefect synchronization.

In conclusion, we performed high-resolution scanning tunneling microscopy of He-ion bombarded single-layer MoS_2 detecting the formation of individual point defects. Line arrays with a width of (8.8 ± 1.7) nm and a pitch of (18.9 ± 2.8) nm were fabricated. We identify oxygen passivated sulfur vacancies as the most abundantly generated defect, and their generation yield agrees quantitatively with numerical simulations. Helium ion beam lithography of 2D materials provides atomistic defect engineering with deterministic control in all three dimensions, enabling top-down fabrication for defect-based single-photon emitters[24] and solid-state quantum circuits.

■ ASSOCIATED CONTENT

Supporting Information

The Supporting Information is available free of charge at https://pubs.acs.org/doi/10.1021/acs.nanolett.0c01222.

Details of the sample preparation process, experimental techniques (HIM, STM/STS, AFM), data treatment, and SRIM/TRIM calculations. Additional data for the STM/STS of line array with highest applied He-ion dose, determination of He-ion spot size, STM image of pristine MoS_2, STM/STS/AFM of oxygen passivated sulfur vacancies, and STS of defects C−F (PDF)

■ AUTHOR INFORMATION

Corresponding Author

Alexander W. Holleitner − *Walter Schottky Institut and Physics Department, Technical University of Munich, 85748 Garching, Germany; Munich Center for Quantum Science and Technology (MCQST), 80799 München, Germany;* orcid.org/0000-0002-8314-4397; Email: holleitner@wsi.tum.de

Authors

Elmar Mitterreiter − *Walter Schottky Institut and Physics Department, Technical University of Munich, 85748 Garching, Germany*

Bruno Schuler − *Molecular Foundry, Lawrence Berkeley National Laboratory, Berkeley, California 94720, United States; nanotech@surfaces Laboratory, Empa − Swiss Federal Laboratories for Materials Science and Technology, 8600 Dübendorf, Switzerland;* orcid.org/0000-0002-9641-0340

Katherine A. Cochrane − *Molecular Foundry, Lawrence Berkeley National Laboratory, Berkeley, California 94720, United States;* orcid.org/0000-0001-8268-2938

Ursula Wurstbauer − *Walter Schottky Institut and Physics Department, Technical University of Munich, 85748 Garching, Germany; Institute of Physics, Westfälische Wilhelms-Universität Münster, 48149 Münster, Germany;* orcid.org/0000-0002-1764-5409

Alexander Weber-Bargioni − *Molecular Foundry, Lawrence Berkeley National Laboratory, Berkeley, California 94720, United States*

Christoph Kastl − *Walter Schottky Institut and Physics Department, Technical University of Munich, 85748 Garching, Germany;* orcid.org/0000-0001-5309-618X

Complete contact information is available at: https://pubs.acs.org/10.1021/acs.nanolett.0c01222

Notes

The authors declare no competing financial interest.

■ ACKNOWLEDGMENTS

The work was supported by Deutsche Forschungsgemeinschaft (DFG) through the German Excellence Strategy via the Munich Center for Quantum Science and Technology (MCQST), EXC-2111-390814868, and e-conversion, EXC 2089/1-390776260. Work at the Molecular Foundry was supported by the Office of Science, Office of Basic Energy Sciences, of the U.S. Department of Energy under contract no. DE-AC02-05CH11231. We gratefully acknowledge support through TUM International Graduate School of Science and Engineering (IGSSE) and the Bavaria California Technology Center (BaCaTeC). We further thank the cluster of excellence Nanosystems Initiative Munich (NIM).

■ REFERENCES

(1) Palacios-Berraquero, C.; Kara, D. M.; Montblanch, A. R.-P.; Barbone, M.; Latawiec, P.; Yoon, D.; Ott, A. K.; Loncar, M.; Ferrari, A. C.; Atatüre, M. Large-Scale Quantum-Emitter Arrays in Atomically Thin Semiconductors. *Nat. Commun.* **2017**, *8* (1), 15093.

(2) Peyskens, F.; Chakraborty, C.; Muneeb, M.; Van Thourhout, D.; Englund, D. Integration of Single Photon Emitters in 2D Layered Materials with a Silicon Nitride Photonic Chip. *Nat. Commun.* **2019**, *10* (1), 4435.

(3) Fuechsle, M.; Miwa, J. A.; Mahapatra, S.; Ryu, H.; Lee, S.; Warschkow, O.; Hollenberg, L. C. L.; Klimeck, G.; Simmons, M. Y. A Single-Atom Transistor. *Nat. Nanotechnol.* **2012**, *7* (4), 242−246.

(4) Awschalom, D. D.; Bassett, L. C.; Dzurak, A. S.; Hu, E. L.; Petta, J. R. Quantum Spintronics: Engineering and Manipulating Atom-Like Spins in Semiconductors. *Science* **2013**, *339* (6124), 1174−1179.

(5) Schröder, T.; Trusheim, M. E.; Walsh, M.; Li, L.; Zheng, J.; Schukraft, M.; Sipahigil, A.; Evans, R. E.; Sukachev, D. D.; Nguyen, C. T.; Pacheco, J. L.; Camacho, R. M.; Bielejec, E. S.; Lukin, M. D.; Englund, D. Scalable Focused Ion Beam Creation of Nearly Lifetime-Limited Single Quantum Emitters in Diamond Nanostructures. *Nat. Commun.* **2017**, *8* (1), 15376.

(6) Ohno, K.; Joseph Heremans, F.; Bassett, L. C.; Myers, B. A.; Toyli, D. M.; Bleszynski Jayich, A. C.; Palmstrøm, C. J.; Awschalom, D. D. Engineering Shallow Spins in Diamond with Nitrogen Delta-Doping. *Appl. Phys. Lett.* **2012**, *101* (8), 082413.

(7) Bayn, I.; Chen, E. H.; Trusheim, M. E.; Li, L.; Schröder, T.; Gaathon, O.; Lu, M.; Stein, A.; Liu, M.; Kisslinger, K.; Clevenson, H.; Englund, D. Generation of Ensembles of Individually Resolvable Nitrogen Vacancies Using Nanometer-Scale Apertures in Ultrahigh-Aspect Ratio Planar Implantation Masks. *Nano Lett.* **2015**, *15* (3), 1751−1758.

(8) Scarabelli, D.; Trusheim, M.; Gaathon, O.; Englund, D.; Wind, S. J. Nanoscale Engineering of Closely-Spaced Electronic Spins in Diamond. *Nano Lett.* **2016**, *16* (8), 4982−4990.

(9) Veligura, V.; Hlawacek, G.; Jahn, U.; van Gastel, R.; Zandvliet, H. J. W.; Poelsema, B. Creation and Physical Aspects of Luminescent Patterns Using Helium Ion Microscopy. *J. Appl. Phys.* **2014**, *115* (18), 183502.

(10) Kern, J.; Niehues, I.; Tonndorf, P.; Schmidt, R.; Wigger, D.; Schneider, R.; Stiehm, T.; Michaelis de Vasconcellos, S.; Reiter, D. E.; Kuhn, T.; Bratschitsch, R. Nanoscale Positioning of Single-Photon Emitters in Atomically Thin WSe_2. *Adv. Mater.* **2016**, *28* (33), 7101−7105.

(11) Branny, A.; Kumar, S.; Proux, R.; Gerardot, B. D. Deterministic Strain-Induced Arrays of Quantum Emitters in a Two-Dimensional Semiconductor. *Nat. Commun.* **2017**, *8* (1), 15053.

(12) Senellart, P.; Solomon, G.; White, A. High-Performance Semiconductor Quantum-Dot Single-Photon Sources. *Nat. Nanotechnol.* **2017**, *12* (11), 1026−1039.

(13) Klein, J.; Lorke, M.; Florian, M.; Sigger, F.; Sigl, L.; Rey, S.; Wierzbowski, J.; Cerne, J.; Müller, K.; Mitterreiter, E.; Zimmermann, P.; Taniguchi, T.; Watanabe, K.; Wurstbauer, U.; Kaniber, M.; Knap, M.; Schmidt, R.; Finley, J. J.; Holleitner, A. W. Site-Selectively Generated Photon Emitters in Monolayer MoS_2 via Local Helium Ion Irradiation. *Nat. Commun.* **2019**, *10* (1), 2755.

(14) Kretschmer, S.; Maslov, M.; Ghaderzadeh, S.; Ghorbani-Asl, M.; Hlawacek, G.; Krasheninnikov, A. V. Supported Two-Dimensional Materials under Ion Irradiation: The Substrate Governs Defect Production. *ACS Appl. Mater. Interfaces* **2018**, *10* (36), 30827−30836.

(15) He, Z.; Zhao, R.; Chen, X.; Chen, H.; Zhu, Y.; Su, H.; Huang, S.; Xue, J.; Dai, J.; Cheng, S.; Liu, M.; Wang, X.; Chen, Y. Defect Engineering in Single-Layer MoS_2 Using Heavy Ion Irradiation. *ACS Appl. Mater. Interfaces* **2018**, *10* (49), 42524−42533.

(16) Hopster, J.; Kozubek, R.; Krämer, J.; Sokolovsky, V.; Schleberger, M. Ultra-Thin MoS_2 Irradiated with Highly Charged Ions. *Nucl. Instrum. Methods Phys. Res., Sect. B* **2013**, *317*, 165−169.

(17) Inoue, A.; Komori, T.; Shudo, K. Atomic-Scale Structures and Electronic States of Defects on Ar^+-Ion Irradiated MoS_2. *J. Electron Spectrosc. Relat. Phenom.* **2013**, *189*, 11−18.

(18) Bell, D. C.; Lemme, M. C.; Stern, L. A.; Williams, J. R.; Marcus, C. M. Precision Cutting and Patterning of Graphene with Helium Ions. *Nanotechnology* **2009**, *20* (45), 455301.

(19) Lemme, M. C.; Bell, D. C.; Williams, J. R.; Stern, L. A.; Baugher, B. W. H.; Jarillo-Herrero, P.; Marcus, C. M. Etching of Graphene Devices with a Helium Ion Beam. *ACS Nano* **2009**, *3* (9), 2674−2676.

(20) Schmidt, M. E.; Muruganathan, M.; Kanzaki, T.; Iwasaki, T.; Hammam, A. M. M.; Suzuki, S.; Ogawa, S.; Mizuta, H. Dielectric-Screening Reduction-Induced Large Transport Gap in Suspended Sub-10 Nm Graphene Nanoribbon Functional Devices. *Small* **2019**, *15* (46), 1903025.

(21) Komsa, H.-P.; Krasheninnikov, A. V. Native Defects in Bulk and Monolayer MoS_2 from First Principles. *Phys. Rev. B: Condens. Matter Mater. Phys.* **2015**, *91* (12), 125304.

(22) Xu, Q.; Wu, M.-Y.; Schneider, G. F.; Houben, L.; Malladi, S. K.; Dekker, C.; Yucelen, E.; Dunin-Borkowski, R. E.; Zandbergen, H. W. Controllable Atomic Scale Patterning of Freestanding Monolayer Graphene at Elevated Temperature. *ACS Nano* **2013**, *7* (2), 1566−1572.

(23) Klein, J.; Kuc, A.; Nolinder, A.; Altzschner, M.; Wierzbowski, J.; Sigger, F.; Kreupl, F.; Finley, J. J.; Wurstbauer, U.; Holleitner, A. W.; Kaniber, M. Robust Valley Polarization of Helium Ion Modified Atomically Thin MoS_2. *2D Mater.* **2018**, *5* (1), 011007.

(24) Klein, J.; Sigl, L.; Gyger, S.; Barthelmi, K.; Florian, M.; Rey, S.; Taniguchi, T.; Watanabe, K.; Jahnke, F.; Kastl, C.; Zwiller, V.; Jöns, K. D.; Müller, K.; Wurstbauer, U.; Finley, J. J.; Holleitner, A. W. Scalable Single-Photon Sources in Atomically Thin MoS_2. *arXiv (Mesoscale and Nanoscale Physics)*, February 20, 2020, 200208819, ver. 1. https://arxiv.org/abs/2002.08819 (accessed on February 25, 2020).

(25) Kastl, C.; Koch, R. J.; Chen, C. T.; Eichhorn, J.; Ulstrup, S.; Bostwick, A.; Jozwiak, C.; Kuykendall, T. R.; Borys, N. J.; Toma, F. M.; Aloni, S.; Weber-Bargioni, A.; Rotenberg, E.; Schwartzberg, A. M. Effects of Defects on Band Structure and Excitons in WS_2 Revealed by Nanoscale Photoemission Spectroscopy. *ACS Nano* **2019**, *13*, 1284−1291.

(26) Shi, T.; Walker, R. C.; Jovanovic, I.; Robinson, J. A. Effects of Energetic Ion Irradiation on WSe_2/SiC Heterostructures. *Sci. Rep.* **2017**, *7* (1), 4151.

(27) Barja, S.; Refaely-Abramson, S.; Schuler, B.; Qiu, D. Y.; Pulkin, A.; Wickenburg, S.; Ryu, H.; Ugeda, M. M.; Kastl, C.; Chen, C.; Hwang, C.; Schwartzberg, A.; Aloni, S.; Mo, S.-K.; Frank Ogletree, D.; Crommie, M. F.; Yazyev, O. V.; Louie, S. G.; Neaton, J. B.; Weber-Bargioni, A. Identifying Substitutional Oxygen as a Prolific Point Defect in Monolayer Transition Metal Dichalcogenides. *Nat. Commun.* **2019**, *10* (1), 3382.

(28) Schuler, B.; Lee, J.-H.; Kastl, C.; Cochrane, K. A.; Chen, C. T.; Refaely-Abramson, S.; Yuan, S.; van Veen, E.; Roldán, R.; Borys, N. J.; Koch, R. J.; Aloni, S.; Schwartzberg, A. M.; Ogletree, D. F.; Neaton, J. B.; Weber-Bargioni, A. How Substitutional Point Defects in Two-Dimensional WS_2 Induce Charge Localization, Spin−Orbit Splitting, and Strain. *ACS Nano* **2019**, *13* (9), 10520−10534.

(29) Hong, J.; Hu, Z.; Probert, M.; Li, K.; Lv, D.; Yang, X.; Gu, L.; Mao, N.; Feng, Q.; Xie, L.; Zhang, J.; Wu, D.; Zhang, Z.; Jin, C.; Ji, W.; Zhang, X.; Yuan, J.; Zhang, Z. Exploring Atomic Defects in Molybdenum Disulphide Monolayers. *Nat. Commun.* **2015**, *6* (1), 6293.

(30) Ouyang, Y.; Ling, C.; Chen, Q.; Wang, Z.; Shi, L.; Wang, J. Activating Inert Basal Planes of MoS_2 for Hydrogen Evolution Reaction through the Formation of Different Intrinsic Defects. *Chem. Mater.* **2016**, *28* (12), 4390−4396.

(31) González, C.; Biel, B.; Dappe, Y. J. Theoretical Characterisation of Point Defects on a MoS_2 Monolayer by Scanning Tunnelling Microscopy. *Nanotechnology* **2016**, *27* (10), 105702.

(32) Aghajanian, M.; Schuler, B.; Cochrane, K. A.; Lee, J.-H.; Kastl, C.; Neaton, J. B.; Weber-Bargioni, A.; Mostofi, A. A.; Lischner, J. Resonant and Bound States of Charged Defects in Two-Dimensional Semiconductors. *Phys. Rev. B: Condens. Matter Mater. Phys.* **2020**, *101* (8), 081201.

(33) *ZEISS ORION NanoFab: Three Ion Beams for Enhanced Flexibility in Sub-10 Nm Fabrication, Product Information*, version 2.0; Carl Zeiss Microscopy GmbH: Oberkochen, Germany.

(34) Pöpsel, C.; Becker, J.; Jeon, N.; Döblinger, M.; Stettner, T.; Gottschalk, Y. T.; Loitsch, B.; Matich, S.; Altzschner, M.; Holleitner, A. W.; Finley, J. J.; Lauhon, L. J.; Koblmüller, G. He-Ion Microscopy as a High-Resolution Probe for Complex Quantum Heterostructures in Core−Shell Nanowires. *Nano Lett.* **2018**, *18* (6), 3911−3919.

(35) Madauß, L.; Ochedowski, O.; Lebius, H.; Ban-d'Etat, B.; Naylor, C. H.; Johnson, A. T. C.; Kotakoski, J.; Schleberger, M. Defect Engineering of Single- and Few-Layer MoS_2 by Swift Heavy Ion Irradiation. *2D Mater.* **2017**, *4* (1), 015034.

(36) Ziegler, J. F.; Biersack, J. P.; Ziegler, M. D.. *SRIM, The Stopping and Range of Ions in Matter*; SRIM Company: Liverpool, NY, 2008.

(37) Klein, J.; Kerelsky, A.; Lorke, M.; Florian, M.; Sigger, F.; Kiemle, J.; Reuter, M. C.; Taniguchi, T.; Watanabe, K.; Finley, J. J.; Pasupathy, A. N.; Holleitner, A. W.; Ross, F. M.; Wurstbauer, U. Impact of Substrate Induced Band Tail States on the Electronic and Optical Properties of MoS_2. *Appl. Phys. Lett.* **2019**, *115* (26), 261603.

(38) Vancsó, P.; Magda, G. Z.; Pető, J.; Noh, J.-Y.; Kim, Y.-S.; Hwang, C.; Biró, L. P.; Tapasztó, L. The Intrinsic Defect Structure of Exfoliated MoS_2 Single Layers Revealed by Scanning Tunneling Microscopy. *Sci. Rep.* **2016**, *6* (1), 29726.

(39) Schuler, B.; Qiu, D. Y.; Refaely-Abramson, S.; Kastl, C.; Chen, C. T.; Barja, S.; Koch, R. J.; Ogletree, D. F.; Aloni, S.; Schwartzberg, A. M.; Neaton, J. B.; Louie, S. G.; Weber-Bargioni, A. Large Spin-Orbit Splitting of Deep In-Gap Defect States of Engineered Sulfur Vacancies in Monolayer WS_2. *Phys. Rev. Lett.* **2019**, *123* (7), 076801.

(40) Mitterreiter, E.; Liang, Y.; Golibrzuch, M.; McLaughlin, D.; Csoklich, C.; Bartl, J. D.; Holleitner, A.; Wurstbauer, U.; Bandarenka, A. S. In-Situ Visualization of Hydrogen Evolution Sites on Helium Ion Treated Molybdenum Dichalcogenides under Reaction Conditions. *Npj 2D Mater. Appl.* **2019**, *3* (1), 25.

(41) Lühmann, T.; John, R.; Wunderlich, R.; Meijer, J.; Pezzagna, S. Coulomb-Driven Single Defect Engineering for Scalable Qubits and Spin Sensors in Diamond. *Nat. Commun.* **2019**, *10* (1), 4956.

(42) Groot-Berning, K.; Kornher, T.; Jacob, G.; Stopp, F.; Dawkins, S. T.; Kolesov, R.; Wrachtrup, J.; Singer, K.; Schmidt-Kaler, F. Deterministic Single-Ion Implantation of Rare-Earth Ions for Nanometer-Resolution Color-Center Generation. *Phys. Rev. Lett.* **2019**, *123* (10), 106802.
(43) Proscia, N. V.; Shotan, Z.; Jayakumar, H.; Reddy, P.; Cohen, C.; Dollar, M.; Alkauskas, A.; Doherty, M.; Meriles, C. A.; Menon, V. M. Near-Deterministic Activation of Room-Temperature Quantum Emitters in Hexagonal Boron Nitride. *Optica* **2018**, *5* (9), 1128.
(44) Hosoki, S.; Hosaka, S.; Hasegawa, T. Surface Modification of MoS_2 Using an STM. *Appl. Surf. Sci.* **1992**, *60−61*, 643−647.
(45) Fox, D. S.; Zhou, Y.; Maguire, P.; O'Neill, A.; Ó'Coileáin, C.; Gatensby, R.; Glushenkov, A. M.; Tao, T.; Duesberg, G. S.; Shvets, I. V.; Abid, M.; Abid, M.; Wu, H.-C.; Chen, Y.; Coleman, J. N.; Donegan, J. F.; Zhang, H. Nanopatterning and Electrical Tuning of MoS_2 Layers with a Subnanometer Helium Ion Beam. *Nano Lett.* **2015**, *15* (8), 5307−5313.
(46) Binnig, G.; Rohrer, H. In Touch with Atoms. *Rev. Mod. Phys.* **1999**, *71* (2), S324−S330.

https://dx.doi.org/10.1021/acs.nanolett.0c01222
Nano Lett. 2020, 20, 4437−4444